Structurally decoupled micromachined gyroscopes with post-release capacitance enhancement

Cenk Acar and Andrei M Shkel

Department of Mechanical and Aerospace Engineering, Microsystems Laboratory,
University of California at Irvine, Engineering Gateway 2110, Irvine, CA 92697, USA

E-mail: cacar@uci.edu and ashkel@uci.edu

Abstract
This paper reports a novel micromachined gyroscope design that provides
enhanced decoupling of the drive and sense modes, and increased actuation
and detection capacitances beyond the fabrication process limitations. The
decoupling mechanism minimizes the effects of fabrication imperfections
and the resulting anisoelasticities, by utilizing independent folded flexures
and constrained moving electrodes in the drive and sense modes. The
post-release capacitance enhancement concept aims to increase the drive and
sense capacitances beyond the minimum gap requirement of the
micromachining process. The approach is based on designing the stationary
components of the electrodes attached to a moving stage that permanently
locks into the desired position before the operation of the device, to
minimize the electrode gap with a simple assembly step.
Bulk-micromachined prototype gyroscopes have been fabricated, and the
experimental results have successfully demonstrated the feasibility of the
design. It is experimentally shown that over an order of magnitude of
capacitance, increase is achieved in the same foot print of the device,
without additional fabrication steps. A noise floor of $0.25°/s/\sqrt{Hz}$ was
demonstrated at 50 Hz bandwidth in atmospheric pressure.

(Some figures in this article are in colour only in the electronic version)

1. Introduction

Gyroscopes are among the most critical components affecting the performance and cost of commercial and military navigation, guidance and vehicle control systems. The complicated dynamics and extremely small detection signals have made gyroscopes one of the most challenging devices to be realized in micromachining, and only a few concepts have succeeded in the market.

Even though an extensive variety of micromachined gyroscope designs and operation principles exist, almost all of the reported micromachined gyroscopes use vibrating mechanical elements to sense angular rate. The concept of utilizing vibrating elements to induce and detect Coriolis force involves no rotating parts that require bearings, and has been proven to be effectively implemented and batch fabricated in different micromachining processes.

The operation principle of the vast majority of all existing micromachined vibratory gyroscopes relies on the generation of a sinusoidal Coriolis force due to the combination of vibration of a proof-mass and an angular-rate input. The proof mass is generally suspended above the substrate by a suspension system consisting of flexible beams. The overall dynamical system is typically a two degrees-of-freedom (2-DOF) mass–spring–damper system, where the rotation-induced Coriolis force causes energy transfer to the sense mode proportional to the angular rate input. In most of the reported micromachined vibratory rate gyroscopes, the proof mass is driven into resonance in the drive direction by an external sinusoidal force. When the gyroscope is subjected to an angular rotation, the sinusoidal Coriolis force at the driving frequency is induced in the direction orthogonal to the drive-mode oscillation and the input angular rate.
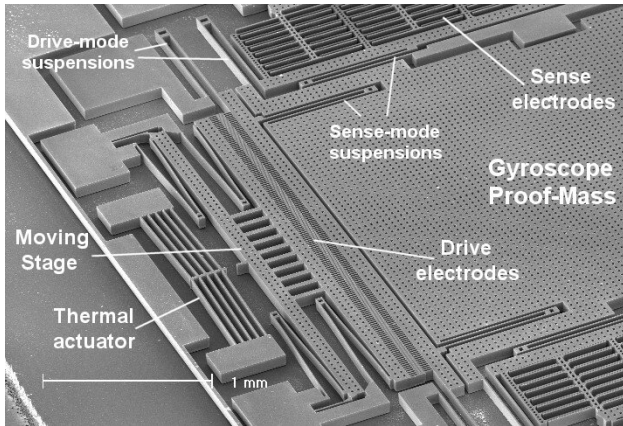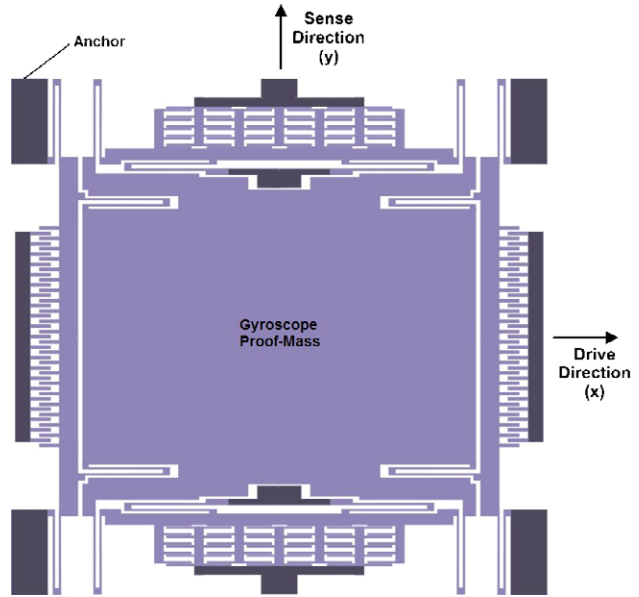
Figure 1. SEM image of the structurally decoupled micromachined gyroscope with post-release capacitance enhancement.

Figure 2. Conceptual schematic of the structurally decoupled micromachined gyroscope.

Fabrication imperfections and residual stresses in MEMS gyroscopes generally introduce small imbalances and asymmetries in the gyroscope suspension structure. Due to lack of perfect alignment of the intended and the actual principle axes of oscillation, anisoelasticity in the gyroscope structure occurs, causing dynamic cross-coupling between the drive and sense directions [16]. This results in mechanical interference between the modes, often much larger than the Coriolis motion. This undesired coupling, called quadrature error, is in phase with the proof-mass displacement, and $90°$ phase shifted from the Coriolis force proportional to the proof-mass velocity. Even though phase-sensitive detection techniques can partially discriminate the quadrature error, the device performance suffers. Various devices have been reported employing mode decoupling mechanisms and independent suspension systems for the drive and sense modes [13, 17–19, 23] in order to suppress the resulting quadrature error due to the coupled oscillation. The micromachined gyroscope structure reported in this paper (figure 1) provides enhanced mechanical decoupling of the drive and sense vibration modes, and completely eliminates the undesired sense-direction excitation force of the drive electrodes due to fabrication imperfections of the actuator. Furthermore, a post-release assembly technique is implemented to enhance the sensing and actuation capacitances beyond the fabrication process limitations.

2. The mode-decoupling structure

The novel decoupling mechanism is based on providing 2-DOF oscillation capability to the gyroscope proof mass, while the degree of freedom of the actuation and detection electrodes are restricted to 1-DOF. This is achieved by structurally decoupling the rotors of the drive and sense electrodes from the proof mass (figures 2 and 3).

In the proposed approach, the moving electrode (rotor) of the drive-mode actuator is directly connected to an anchor point through a folded suspension beam (figure 2). The folded suspension completely restricts the sense-direction motion, and forces the drive-mode electrode rotor to oscillate purely in the drive direction. Thus, the undesired electrostatic force

generated in the sense direction by the drive electrodes due to fabrication imperfections is drastically suppressed. Also, the lateral stability of the actuation electrodes is significantly enhanced.

The drive-mode excitation force is applied to the gyroscope proof mass through a folded suspension, which directly transfers the drive-mode oscillation of the drive electrode rotor, while allowing the proof mass to oscillate independently in the sense direction.

Similarly, the moving electrode of the sense capacitors is directly connected to an anchor point through a folded suspension beam (figure 2). Thus, transfer of the drive-mode oscillations of the gyroscope proof mass to the sense electrodes is completely eliminated. The sense-mode oscillations of the proof mass due to the rotation-induced Coriolis force are directly transferred to the sense-electrode rotor through another folded beam, which also allows relative drive-mode oscillations.

Thus, the benefits of the structural decoupling mechanism can be summarized as follows:

- The mechanical coupling between the drive and sense modes is minimized. Thus, zero-rate-output and quadrature error are significantly reduced in the presence of structural imperfections.
- Due to fabrication imperfections and asymmetries, drive electrodes generally generate undesired electrostatic forces in the sense direction that excite the sense mode. The structure drastically suppresses the effect of this parasitic force.
- The sensing electrodes do not respond to the drive-mode vibrations owing to the structural decoupling. The spurious capacitance changes in the sense electrodes due to the drive mode oscillations, and the resulting error signal $90°$ phase shifted from the Coriolis signal is minimized.
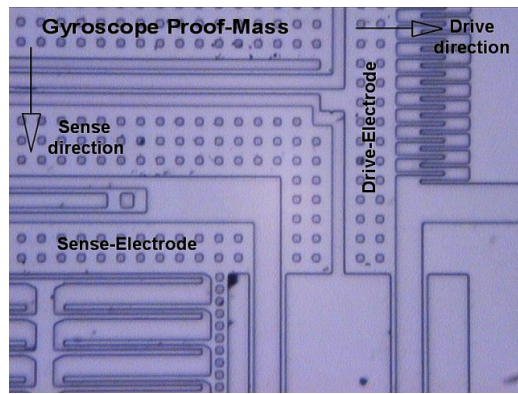
(a)
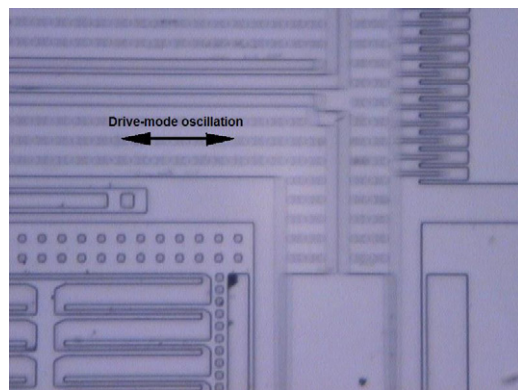
(b)
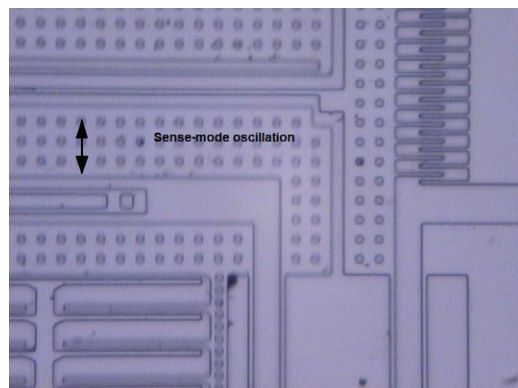
(c)

Figure 3. (a) Microscope photograph of the mode-decoupling structure. (b) The drive-mode oscillations (blurred), where only the drive-electrode rotor deflects. (c) The sense-mode oscillations (blurred), where only the sense-electrode rotor deflects.

3. Post-release capacitance enhancement

In micromachined inertial sensors, capacitive sensing and actuation offer several benefits when compared to other sensing and actuation means (piezoresistive, piezoelectric, optical, magnetic, etc) with their ease of fabrication and integration, good dc response and noise performance, high sensitivity, low drift and low temperature sensitivity.

The performance of micromachined sensors employing capacitive detection is generally determined by the nominal capacitance of the sensing electrodes. Even though increasing the overall sensing area provides improved sensing
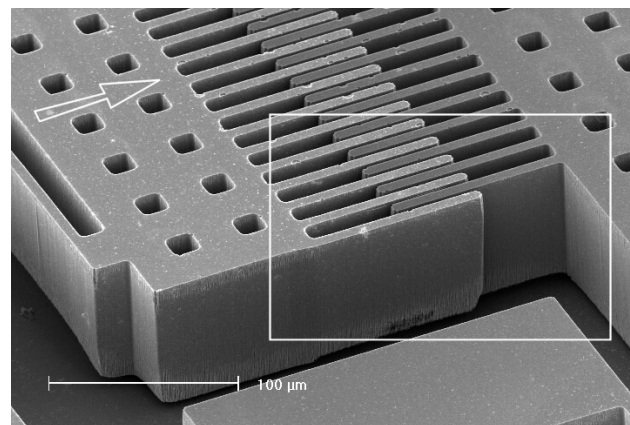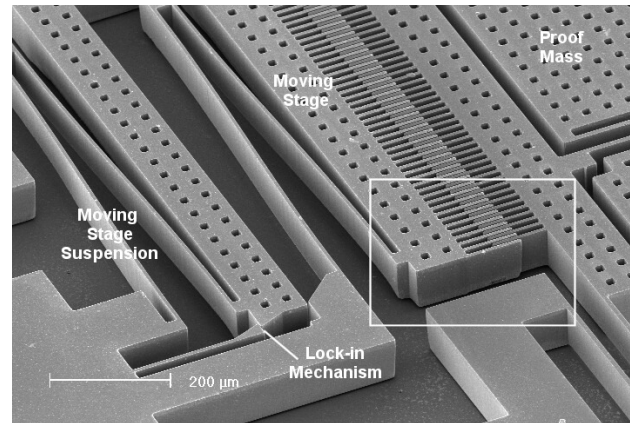
Figure 4. SEM images of post-release positioned comb drives integrated in a micromachined gyroscope. The resulting finger gap after the assembly is 1 μm, while the process minimum-gap requirement is 10 μm.

capacitance, the sensing electrode gap is the foremost factor that defines the upper bound. Similarly, the force generated by the electrostatic actuation electrodes (comb drives or parallel plates) is limited by the minimum gap attainable in the fabrication process. In electrostatically actuated devices such as micromachined gyroscopes, the nominal actuation capacitance determines the required drive voltages. For a small actuation capacitance, large voltages are needed to achieve sufficient forces, which in turn results in a large drive signal feed-through.

Various advanced fabrication technologies have been reported to minimize electrode gap, based on deposition of thin layers on electrode sidewalls [1, 2, 5]. For example, in one reported approach, high aspect-ratio polysilicon structures are created by refilling deep trenches with polysilicon deposited over a sacrificial oxide layer. Thick single-crystal silicon structures are released from the substrate through the front side of the wafer by means of a combined directional and isotropic silicon dry etch and are protected on the sides by refilled trenches. This process involves one layer of low-pressure chemical vapor deposited (LPCVD) silicon nitride, one layer of LPCVD silicon dioxide and one layer of LPCVD polysilicon [2]. This process and similar approaches require additional fabrication steps.

The post-release assembly technique presented in this paper aims to increase the sensing and actuation capacitances
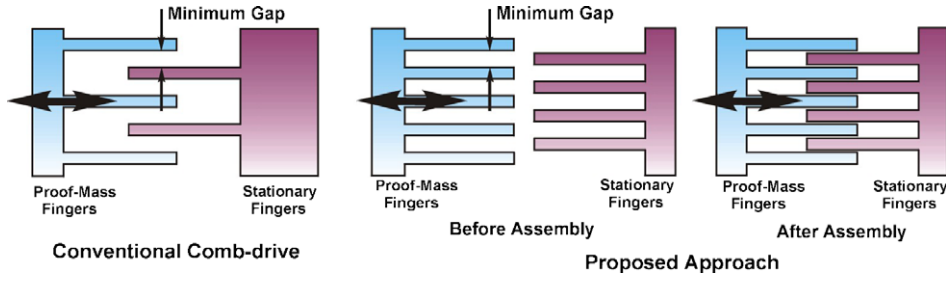
Figure 5. Comparison of a conventional comb-drive structure, and the post-release positioning approach designed for the same fabrication process. Note the difference in the resulting gap, and the number of fingers per unit area.

in micromachined devices, without any modification of the fabrication process. With a simple additional assembly step, the performance and noise characteristics are enhanced beyond the fabrication process limitations.

### 3.1. Enhancement of comb-drive capacitance

Interdigitated comb drives are one of the most common actuation structures used in MEMS devices, and are utilized for actuation in the proposed device. The primary advantages of comb drives are long-stroke actuation capability, the linearity of the generated forces and the ability of applying displacement-independent forces for high-stability actuators. With a balanced interdigitated comb-drive scheme imposed by applying $V_1 = V_{dc} + v_{ac}$ to one set of comb drives and $V_2 = V_{dc} - v_{ac}$ to the other set, the net electrostatic force reduces to [11]

$$F_{comb} = 4 \frac{\varepsilon_0 z_0 N}{y_0} V_{dc} v_{ac}, \tag{1}$$

where V_{dc} is the dc bias voltage, v_{ac} is the sinusoidal ac voltage, z_0 is the finger thickness and y_0 is the finger separation. In conventional interdigitated comb drives, the gap between each stationary and moving finger is determined by the minimum-gap requirement of the fabrication process (figure 5). For example, if the minimum gap is 10 μm, the gap between the conventional comb-drive fingers is 10 μm.

In the presented post-release positioning approach, the fingers attached to opposing electrodes are designed initially apart, and interdigitated after the release. Thus, the gap between the fingers after interdigitating can be much smaller than the minimum-gap requirement (figure 5). For the same example, if the width of one finger is 8 μm and the minimum gap is 10 μm, the resulting gap between the stationary and moving fingers after the assembly is 1 μm. This results in a ten times increase in the force per finger. Furthermore, the number of fingers per unit area is increased by allowing smaller gaps. In this example, exactly two times as many fingers can be used in the same area, resulting in a total of 20 times increase in the drive force.

Figures 4 and 6 present microscope photographs of the assembled post-release positioning comb drives integrated in the decoupled micromachined gyroscope. It is observed that excellent positioning is achieved, providing uniform gaps across the comb-drive structure. The gyroscope proof mass is successfully driven into resonance in the drive mode with the assembled comb fingers (figure 7). In the presented device, thermal actuators have been used (figure 9) for displacing and


(a)

(b)
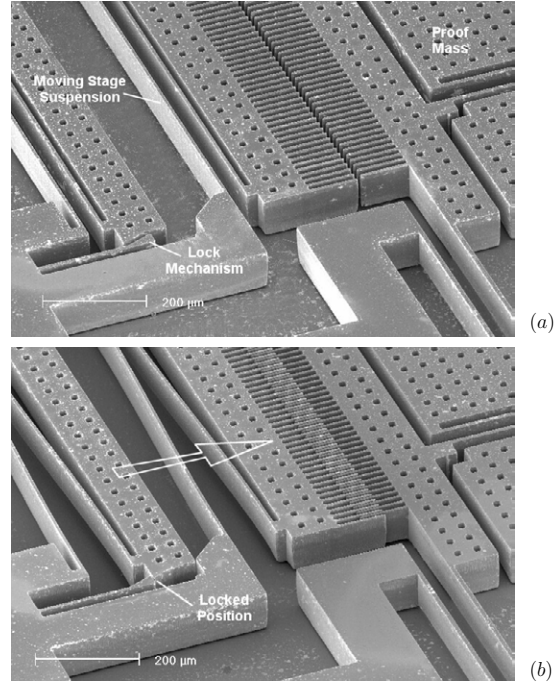
Figure 6. SEM images of post-release positioning comb drives integrated in a micromachined gyroscope, (a) before and (b) after assembly.
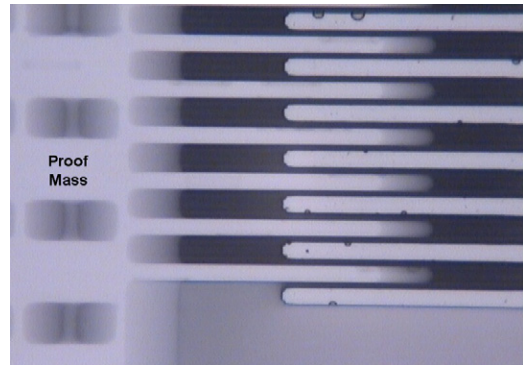

Figure 7. Microscope photographs of the assembled post-release positioning comb drives integrated in a micromachined gyroscope. The gyroscope is successfully driven into resonance in the drive mode with the assembled comb fingers.

assembling the moving stages. Bistable locking mechanisms and self-assembly approaches have also been explored (figure 8) [3].

1095
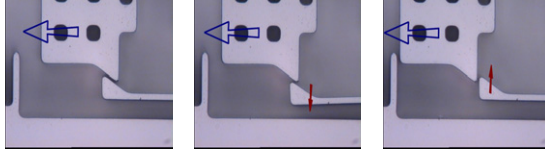
Figure 8. Microscope photographs of the ratchet structure utilized as the locking mechanism for post-release positioning.

Before Assembly

During Assembly

After Assembly
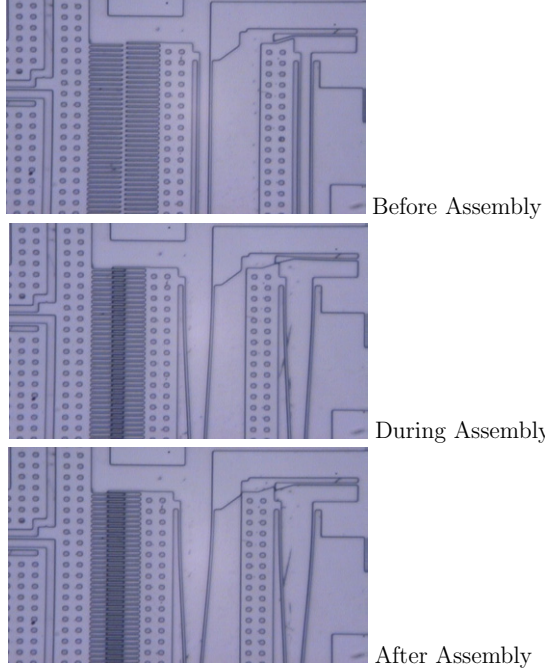
Figure 9. The assembly sequence of the post-release positioning comb drives using thermal actuators.

3.2. Enhancement of parallel-plate capacitance

Parallel-plate actuation provides much larger forces per unit area compared to comb drives, with the expense of limited stable actuation range, and nonlinear actuation forces. The net force generated by a parallel-plate actuator is

$$\vec{F}_{pp} = -\frac{\varepsilon_0 V_{dc}^2 z_0 x_0}{2(d_0 - x)^2} \hat{e}_y, \qquad (2)$$

where $\varepsilon_0 = 8.854 \times 10^{-12}$ F m^{-1} is the dielectric constant, A is the total actuation area, d_0 is the electrode gap and V_{dc} is the dc bias voltage. The nonlinear electrostatic force profile in parallel-plate actuation electrodes is usually exploited for resonance frequency tuning. The negative electrostatic spring constant that reduces the resonant frequency with increasing dc bias can be found by taking the derivative of the electrostatic force F_{pp} with respect to displacement

$$k_{el} = \frac{\partial F_{pp}}{\partial x} = -\frac{\varepsilon_0 A}{d_0^3} V_{dc}^2. \qquad (3)$$

Thus, the shrinking of the electrode gap enhances both the actuation force and the electrostatic frequency tuning range.

3.2.1. Capacitive detection.
In micromachined inertial sensors, differential capacitance sensing is generally employed to enhance and linearize the capacitance change with
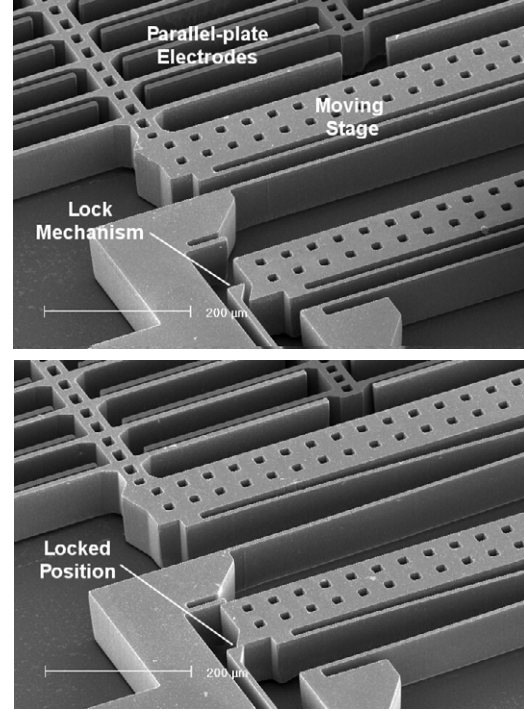
Figure 10. SEM images of post-release positioning sensing electrodes integrated in a micromachined gyroscope, before and after assembly.

deflection. Defining y_0 as the finger separation, l as the length of the fingers and t as the thickness of the fingers, the differential capacitance values become

$$C_{s\pm} = N \frac{\varepsilon_0 t l}{y_0 \mp y}, \qquad \Delta C = C_{s+} - C_{s-} = 2N \frac{\varepsilon_0 t l}{y_0^2} y. \quad (4)$$

It is observed that the capacitance change is inversely proportional to the square of the initial gap. Thus, the performance of the sensor (i.e. sensitivity, resolution and signal-to-noise ratio) is improved quadratically by decreasing the initial gap of the sensing electrodes.

Similarly, the post-release positioning concept is implemented in parallel-plate detection electrodes by attaching the stationary fingers of the sensing electrodes to a moving stage that locks into the desired position before operation. Figure 10 presents scanning-electron-microscope images of the post-release positioning sensing electrodes integrated in a micromachined gyroscope, before and after assembly. It is observed that excellent positioning is achieved, providing uniform gaps across the sensing electrode structure. Electrode gaps in the order of 1–2 μm have been achieved with 100 μm thick structures (figure 11), while the minimum-gap requirement of the fabrication process is 10 μm.

4. Experimental results

4.1. Fabrication of prototypes

The structurally decoupled micromachined gyroscope design concept with post-release capacitance enhancement was analyzed experimentally on the bulk-micromachined prototype structures, fabricated in the UCI Integrated Nano-Systems Research Facility. For the fabrication of prototypes,
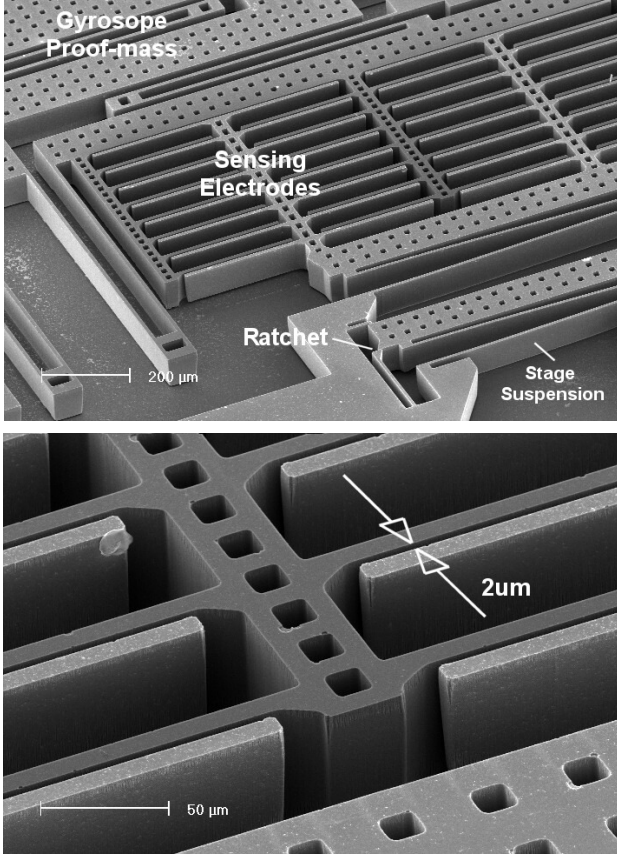
Figure 11. Electrode gaps in the order of 1–2 μm have been achieved with 100 μm thick structures, while the minimum-gap requirement of the fabrication process is 10 μm.

a one-mask process was developed, based on deep-reactive ion etching (DRIE) through the 100 μm device layer of SOI (silicon-on-insulator) wafers, and front-side release of the structures by etching the oxide layer in HF solution. The DRIE process was performed in an STS ICP, using an 8 s etch step cycle with 130 sccm SF_6 and 13 sccm O_2, 600 W coil power and 15 W platen power; and 5 s passivation step cycle time with 85 sccm C_4F_6, 600 W coil power and 0 W platen power. In the device, 15 μm $\times$ 15 μm holes were used to perforate the suspended structures, and 10 μm gaps were used in the sensing and actuation electrodes. The lowest etch rates were observed for the 15 μm $\times$ 15 μm holes, at approximately 1.25 μm min^{-1}, and 85 min DRIE time was used to assure complete through-etch while minimizing excessive undercutting in larger areas. The anchors were designed as unperforated areas larger than 40 μm $\times$ 40 μm for 25 min release in 49% HF solution.

4.2. System identification

The fabricated prototype devices were characterized in the UCI MicroSystems laboratory. The drive- and sense-mode frequency responses were experimentally acquired by electrostatic excitation with a sinusoidal signal in frequency sweep mode and simultaneous capacitive detection. In practice, the acquired frequency response signal is generally corrupted (figure 12) by the feed-through of the excitation

signal to the output signal over a lumped parasitic capacitance C_p between the bonding pads and the substrate, and a finite substrate resistance R_p in parallel to the ideal system dynamics (figure 13).

Although the corrupted frequency response could be used to obtain a rough approximation of the system parameters, close estimation of parameters, even the resonance frequency, is not possible. Fortunately, the ideal system response can be extracted from the corrupted response based on the analysis of the real and imaginary components of the response. The transfer function of the overall system, and the real and imaginary parts of the frequency response are

$$\frac{V_o}{V_{in}} = K\frac{\alpha s}{ms^2 + cs + k} + K\frac{C_p s}{R_p C_p s + 1},$$

$$\text{Re}\left(\frac{V_o}{V_{in}}\right) = \frac{K\alpha c\omega^2}{(k - m\omega^2)^2 + c^2\omega^2} + \frac{K R_p C_p^2 \omega^2}{(R_p C_p \omega)^2 + 1},$$

$$\text{Im}\left(\frac{V_o}{V_{in}}\right) = \frac{K\alpha(k - m\omega^2)\omega}{(k - m\omega^2)^2 + c^2\omega^2} + \frac{K C_p \omega}{(R_p C_p \omega)^2 + 1},$$

where K is the transimpedance amplifier gain, and $\alpha = \frac{1}{2}\frac{\partial C_{drive}}{\partial x}V_{dc} \times \frac{\partial C_{sense}}{\partial x}V_{dc}$ contains the coefficients for conversion of the input sine wave to the mechanical force, and the mechanical displacement to the motion induced current. The exact mechanical resonance point is very easily identified from real part of the response, since the real part reaches its maximum at the resonant frequency $\omega_n = \sqrt{\frac{k}{m}}$ regardless of the parasitics.

The real part of the response includes only the parasitic effects at frequencies away from the resonance point, and the imaginary part of an ideal system's response is zero at the resonance point. Evaluating the real part at one frequency ω_l away from ω_n, and the imaginary part at ω_n yields two nonlinear equations with two unknowns R_p and C_p,

$$\text{Re}\left[\frac{V_o}{V_{in}}(\omega_l)\right] = \frac{R_p C_p^2 \omega_l^2}{(R_p C_p \omega_l)^2 + 1},$$

$$\text{Im}\left[\frac{V_o}{V_{in}}(\omega_n)\right] = \frac{C_p \omega_n}{(R_p C_p \omega_n)^2 + 1}.$$

These two equations are solved simultaneously to identify the values of R_p and C_p. Evaluating the real part at the resonance point, and the imaginary part of the response slightly away from resonance (ω_m) yields two equations for the two unknowns α and c,

$$\text{Re}\left[\frac{V_o}{V_{in}}(\omega_n)\right] = \frac{\alpha}{c} + \frac{R_p C_p^2 \omega_n^2}{(R_p C_p \omega_n)^2 + 1},$$

$$\text{Im}\left[\frac{V_o}{V_{in}}(\omega_m)\right] = \frac{\alpha(k - m\omega_m^2)\omega}{(k - m\omega_m^2)^2 + c^2\omega_m^2} + \frac{C_p \omega_m}{(R_p C_p \omega_m)^2 + 1}.$$

Solving these two equations simultaneously, the values of the electrical gain α and the damping coefficient c are identified, yielding an accurate estimation of the Q factor and the bandwidth. Figure 12 shows the experimentally acquired response with the parasitics, and the simulated response of the identified model. It is observed that the system parameters and the parasitics are effectively identified with the presented

Experimental Drive-Mode Response (with parasitics)
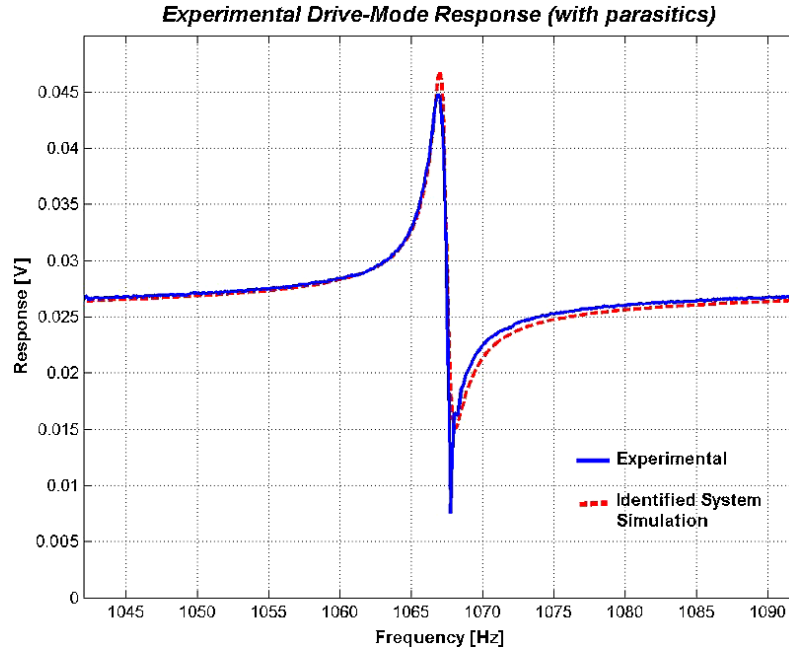
Figure 12. The measured drive-mode frequency response, corrupted by the drive feed-through signal. The system parameters and the parasitics are effectively identified with the presented algorithm, and the simulated response of the identified system closely matches the experimental data.
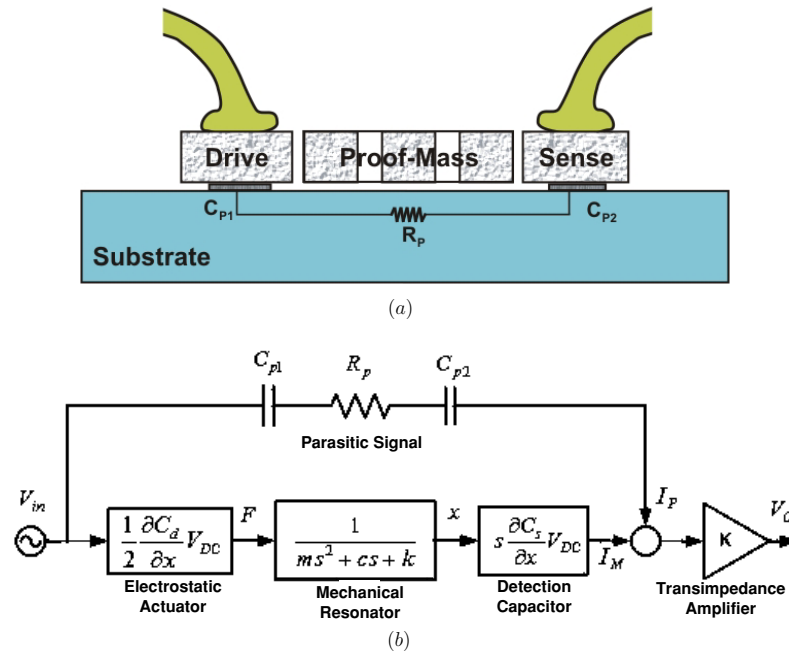
Figure 13. (*a*) The parasitic signal runs over the parasitic capacitances through the substrate. (*b*) The transfer function model of the overall system, including the lumped parasitic capacitance, and the substrate resistance.

algorithm, and the simulated response of the identified system closely matches the experimental data. For the oscillator mass of 2.31×10^{-6} kg, the identified parameters are $C_p = 7.62$ pF, $R_p = 2.449$ MΩ, and $\alpha = 2.226 \times 10^{-13}$ (V F m^{-1})^2 with 6 V dc voltage. This yields $\frac{\partial C_d}{\partial x} = 1.112 \times 10^{-7}$ F m^{-1}.

When an identical gyroscope structure employing conventional comb drives with 10 μm gaps was characterized with the same technique, the system identification algorithm yielded $\frac{\partial C_d}{\partial x} = 1.54 \times 10^{-8}$ F m^{-1}. This experimentally demonstrates that 7.22 times larger actuation force is

achieved with the post-release capacitance enhancement method compared to conventional comb drives.

Having identified the parasitic terms in the real and imaginary parts of the response, these terms can be numerically filtered from the measured signal to reflect the actual mechanical dynamics, by subtracting the evaluated parasitic term at each frequency from the acquired trace. Figure 14 presents the amplitude and phase of the experimentally acquired frequency response at 250 mTorr pressure with numerical filtering of parasitics.
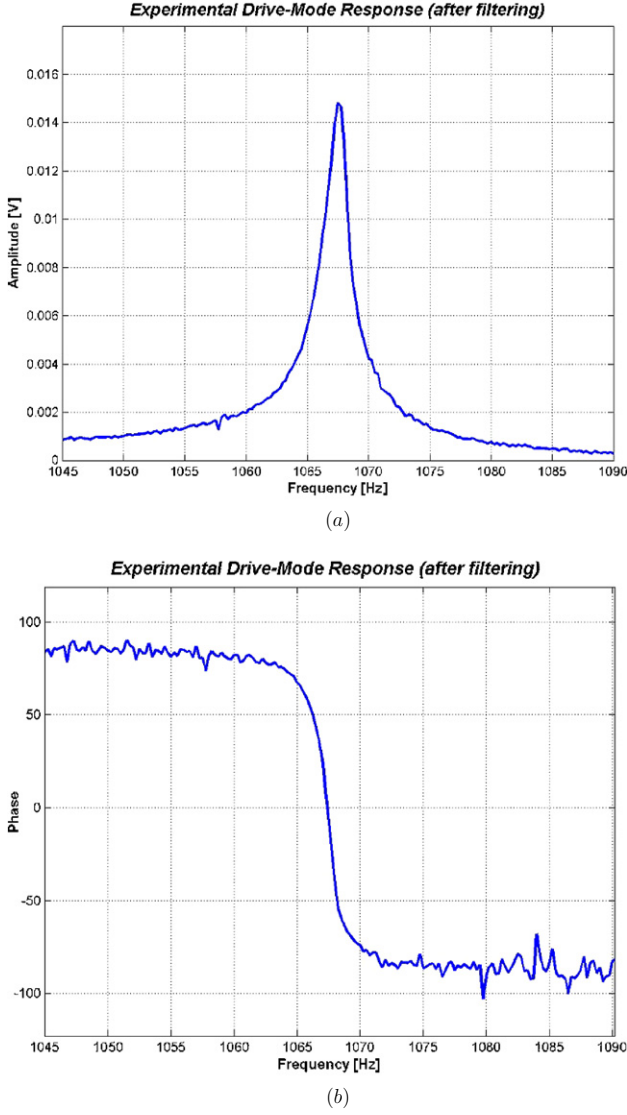
Figure 14. Experimental measurements of the drive-mode frequency response, with numerical filtering of the parasitics.
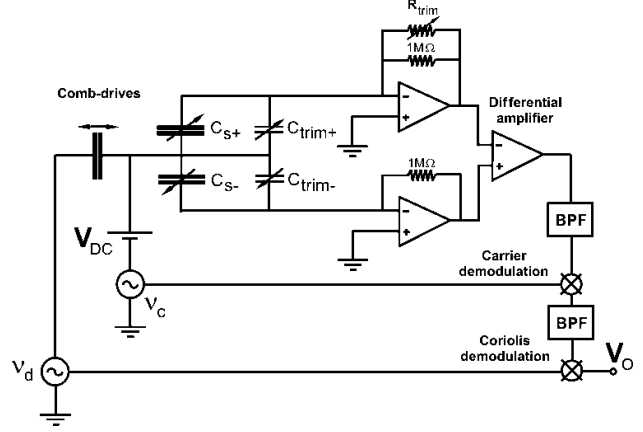

Figure 15. The circuit-level model of the synchronous demodulation technique, including the trimming capacitors for capacitance matching.

4.3. Rate-table characterization

The synchronous demodulation technique was used to detect the Coriolis response of the gyroscope proof mass in the sense mode. A high-frequency carrier signal was imposed on the structure, which is the common mode of the differential capacitive bridge in the sense mode. The current output from each sensing capacitor due to the carrier signal was converted into a voltage signal and amplified. The difference of the outputs was amplitude demodulated at the carrier signal frequency, yielding the Coriolis response signal at the driving frequency (figure 15).

This scheme can be modeled as a sinusoidal carrier signal V_c imposed over the variable sensing capacitor C_s, and the sense current is amplitude modulated by the change in capacitance. The carrier signal and the sensing capacitance will then be of the form

$$V_c = \upsilon_c \sin \omega_c t \qquad (5)$$

$$C_s = C_{sn} + C_{so} \sin \omega_d t, \qquad (6)$$

where C_{sn} is the nominal sensing capacitance, C_{so} is the amplitude of capacitance change due to the Coriolis response, ω_d is the driving frequency (and thus, the sense-mode oscillation frequency) and ω_c is the carrier signal frequency. Thus, the sense current becomes

$$i_s = \frac{\mathrm{d}}{\mathrm{d}t}[V_c(t)C_s(t)]$$

$$= \frac{\mathrm{d}}{\mathrm{d}t}[C_{sn}\upsilon_c \sin \omega_c t + C_{so}\upsilon_c \sin \omega_c t \sin \omega_d t]. \qquad (7)$$

The sense current is amplified by the trans-impedance amplifier with a gain of K, and converted into a voltage signal V_s,

$$V_s = K\omega_c C_{sn}\upsilon_c \cos \omega_c t + \frac{KC_{so}\upsilon_c}{2}[(\omega_c + \omega_d)\sin(\omega_c + \omega_d)t$$
$$- (\omega_c - \omega_d)\sin(\omega_c - \omega_d)t].$$

V_s is then amplitude demodulated at the carrier frequency ω_c. By multiplying the sense signal V_s with a sinusoidal signal at ω_c, the amplitude demodulated signal V_{sd} is obtained as

$$V_{sd} = K\omega_c C_{sn}\upsilon_c \cos \omega_c t \sin \omega_c t$$
$$+ \tfrac{1}{2}KC_{so}\upsilon_c[(\omega_c + \omega_d)\sin(\omega_c + \omega_d)t \sin \omega_c t$$
$$- (\omega_c - \omega_d)\sin(\omega_c - \omega_d)t \sin \omega_c t]$$

and after regrouping the corresponding terms,

$$V_{sd} = \tfrac{1}{2}K\omega_c C_{sn}\upsilon_c \sin 2\omega_c t$$
$$+ \tfrac{1}{4}KC_{so}\upsilon_c(\omega_c + \omega_d)[\cos \omega_d t - \cos(2\omega_c + \omega_d)t]$$
$$- \tfrac{1}{4}KC_{so}\upsilon_c(\omega_c - \omega_d)[\cos \omega_d t - \cos(2\omega_c - \omega_d)t].$$

When the amplitude demodulated signal V_{sd} is band-pass filtered at the drive frequency ω_d, the high-frequency signals at $2\omega_c$, $(2\omega_c + \omega_d)$ and $(2\omega_c - \omega_d)$ are attenuated, leaving
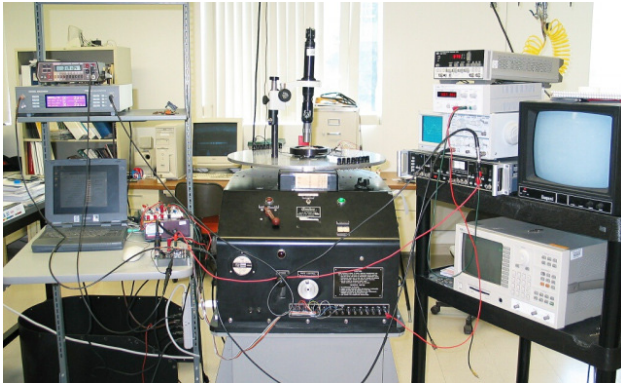
$$V_{sd} = \tfrac{1}{2}K\omega_d C_{so}\upsilon_c \cos \omega_d t. \qquad (8)$$

When the signal V_{sd} is further amplitude demodulated at the driving frequency using the drive signal as the reference signal, the output voltage proportional to the angular rate input is obtained as
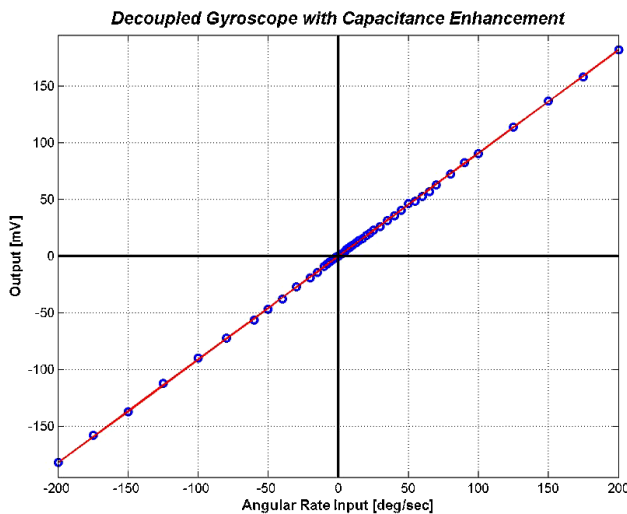
$$V_o = \tfrac{1}{2}K\omega_d C_{so}\upsilon_c. \qquad (9)$$

In the practical implementation of the synchronous demodulation technique, the imbalance in the parasitic

Figure 16. The experimental setup utilized for rate-table characterization of prototype gyroscopes.

Figure 17. The angular-rate input versus voltage output plot obtained from the structurally decoupled gyroscopes with the post-release assembled comb drives and sensing electrodes.

capacitances of the sense-mode differential capacitive bridge results in a large dc offset, corrupting the Coriolis signal. Utilizing trimming capacitors in parallel to the capacitors in the differential capacitive bridge, capacitance matching is achieved, and the dc offset is nulled.

During the rate-table characterization, a 2 Vrms carrier signal at 20 kHz was imposed on the gyroscope structure with 10 V dc bias. The current output from each sensing capacitor due to the carrier signal was converted into a voltage signal and amplified using two transimpedance amplifiers with 1 MΩ feedback resistors. A lock-in amplifier was utilized to provide the 1 V ac drive signal, and to synchronously demodulate the difference of the transimpedance amplifier outputs at the drive frequency in the internal reference mode. The drive-mode amplitude was measured optically as 12 μm in atmospheric pressure (figure 16).

Using the synchronous demodulation technique, a sensitivity of 0.921 mV s/° (figure 17) and a noise floor of 0.231 mV/$\sqrt{\text{Hz}}$ at 50 Hz bandwidth was measured. This yields a measured resolution of 0.25°/s/$\sqrt{\text{Hz}}$ at 50 Hz bandwidth, with the post-release assembled comb drives and sensing electrodes.

5. Conclusion

The post-release capacitance enhancement technique has been successfully implemented in the comb drives and the sensing electrodes of bulk-micromachined prototype structurally decoupled gyroscopes. System identification algorithms applied to the electrostatically acquired drive-mode frequency responses of the gyroscope revealed that 7.22 times larger actuation force is achieved compared to conventional comb drives implemented in the exact same gyroscope structure. With the assembled comb drives, 12 μm drive amplitude was achieved with 10 V dc and 1 V ac actuation voltages in air. The gyroscope with assembled comb drives and detection electrodes exhibited a sensitivity of 0.91 mV s/°, excellent linearity, and a noise floor of 0.25°/ s/$\sqrt{\text{Hz}}$ at 50 Hz bandwidth in atmospheric pressure.

References

[1] Hirano T, Furuhata T, Gabriel K J and Fujita H 1992 Design, fabrication and operation of submicron gap comb-drive microactuators *J. Microelectromech. Syst.* **1** 52–9

[2] Ayazi F and Najafi K 2000 High aspect-ratio combined poly and single-crystal silicon (HARPSS) MEMS technology *J. Microelectromech. Syst.* **9** 288–94

[3] Acar C and Shkel A 2004 Post-release capacitance enhancement in micromachined devices *IEEE Sensors Conf. (Vienna, Austria, October 2004)*

[4] Acar C 2004 Robust micromachined vibratory gyroscopes *PhD Thesis* University of California Irvine

[5] Pourkamali S and Ayazi F 2003 SOI-based HF and VHF single-crystal silicon resonators with sub-100 nanometer vertical capacitive gaps *Proc. Solid-State Sensor and Actuator Workshop*

[6] Clark W A, Howe R T and Horowitz R 1994 Surface micromachined Z-axis vibratory rate gyroscope *Solid-State Sensor and Actuator Workshop*

[7] Barbour N and Schmidt G 2001 Inertial sensor technology trends *IEEE Sensors J.* **1** 332–9

[8] Yazdi N, Ayazi F and Najafi K 1998 Micromachined inertial sensors *Proc. IEEE* **86** 1640–58

[9] http://www.analogdevices.com

[10] Alper S E and Akin T 2000 A planar gyroscope using standard surface micromachining process *Conf. Solid-State Transducers (Copenhagen, Denmark)* pp 387–90

[11] Clark W A, Howe R T and Horowitz R 1994 Surface micromachined Z-axis vibratory rate gyroscope *Proc. Solid-State Sensor and Actuator Workshop (June 1994)* pp 199–202

[12] Hong Y S, Lee J H and Kim S H 2000 A laterally driven symmetric micro-resonator for gyroscopic applications *J. Micromech. Microeng.* **10** 452–8

[13] Alper S E and Akin T 2002 A symmetric surface micromachined gyroscope with decoupled oscillation modes *Sensors Actuators* A **97** 347–58

[14] Park S and Horowitz R 2001 Adaptive control for Z-axis MEMS gyroscopes *American Control Conf. (Arlington, VA, June 2001)*

[15] Shkel A, Horowitz R, Seshia A, Park S and Howe R T 1999 Dynamics and control of micromachined gyroscopes *American Control Conf. (CA)* pp 2119–24

[16] Shkel A, Howe R T and Horowitz R 1999 Modeling and simulation of micromachined gyroscopes in the presence of imperfections *Int. Conf. on Modeling and Simulation of Microsystems (Puerto Rico)* pp 605–8

[17] Geen J A 1998 A path to low cost gyroscopy *Solid-State Sensor and Actuator Workshop (Hilton Head, SJ)* pp 51–4

[18] Geiger W *et al* 2001 Decoupled microgyros and the design principle DAVED *IEEE Sensors J.* 170–3

[19] Mochida Y *et al* 2000 A micromachined vibrating rate gyroscope with independent beams for drive and detection modes *Sensors Actuators* A **80** 170–8

[20] Geen J A and Carow D W 2000 Micromachined gyros *US Patent* 6,122,961

[21] Hsu Y W 1999 Multi-element microd gyro *US Patent* 6,089,089

[22] Boser B E 1997 Electronics for micromachined inertial sensors *Proc. Transducers*

[23] Niu M, Xue W, Wang X, Xie J, Yang G and Wang W 1997 Design and characteristics of two-gimbals micro-gyroscopes fabricated with quasi-LIGA process *Int. Conf. on Solid-State Sensor and Actuators* pp 891–4